The energetics of starburst-driven outflows at $z \sim 1$ from KMOS

A. M. Swinbank,[1,*] C. M. Harrison,[1,2] A. L. Tiley,[1] H. L. Johnson,[1] Ian Smail,[1] J. P. Stott,[3] P. N. Best,[6] R. G. Bower,[1] M. Bureau,[4] A. Bunker,[4] M. Cirasuolo,[2] M. Jarvis,[4] G. E. Magdis,[5] R. M. Sharples,[1] & D. Sobral[3]

[1] *Institute for Computational Cosmology, Durham University, South Road, Durham, DH1 3LE, UK*
[*] *Email: a.m.swinbank@dur.ac.uk*
[2] *European Southern Observatory, Karl-Schwarzschild-Str. 2, 85748 Garching b. München, Germany*
[3] *Department of Physics, Lancaster University, Lancaster, LA1 4YB, U.K.*
[4] *Sub-dept. of Astrophysics, Department of Physics, University of Oxford, Denys Wilkinson Building, Keble Road, Oxford, OX1 3RH, U.K.*
[5] *Cosmic DAWN Centre, Niels Bohr Institute, University of Copenhagen, Juliane Mariesvej 30, 2100, Copenhagen, Denmark*
[6] *Institute for Astronomy, University of Edinburgh, Royal Observatory, Edinburgh EH9 3HJ*

8 May 2019

ABSTRACT

We present an analysis of the gas outflow energetics from KMOS observations of ~ 529 main-sequence star-forming galaxies at $z \sim 1$ using broad, underlying Hα and forbidden lines of [NII] and [SII]. Based on the stacked spectra for a sample with median star-formation rates and stellar masses of SFR $= 7 \, \mathrm{M}_\odot$ / yr and $M_\star = (1.0 \pm 0.1) \times 10^{10} \, \mathrm{M}_\odot$ respectively, we derive a typical mass outflow rate of $\dot{M}_{\mathrm{wind}} = 1$–$4 \, \mathrm{M}_\odot \, \mathrm{yr}^{-1}$ and a mass loading of $\dot{M}_{\mathrm{wind}}$ / SFR $= 0.2$–0.4. By comparing the kinetic energy in the wind with the energy released by supernovae, we estimate a coupling efficiency between the star formation and wind energetics of $\epsilon \sim 0.03$. The mass loading of the wind does not show a strong trend with star-formation rate over the range ~ 2–$20 \, \mathrm{M}_\odot \, \mathrm{yr}^{-1}$, although we identify a trend with stellar mass such that $d\mathrm{M}$ / dt / SFR $\propto \mathrm{M}_\star^{0.26 \pm 0.07}$. Finally, the line width of the broad Hα increases with disk circular velocity with a sub-linear scaling relation $\mathrm{FWHM}_{\mathrm{broad}} \propto v^{0.21 \pm 0.05}$. As a result of this behavior, in the lowest mass galaxies ($\mathrm{M}_\star \lesssim 10^{10} \, \mathrm{M}_\odot$), a significant fraction of the outflowing gas should have sufficient velocity to escape the gravitational potential of the halo whilst in the highest mass galaxies ($\mathrm{M}_\star \gtrsim 10^{10} \, \mathrm{M}_\odot$) most of the gas will be retained, flowing back on to the galaxy disk at later times.

Key words: galaxies: starburst, galaxies: evolution, galaxies: high-redshift

1 INTRODUCTION

The process by which massive stars release energy and mass back into the interstellar medium (ISM) is critical to the evolution of galaxies. Theoretical models suggest that "superwinds" result when the energy injection rate from supernovae and stellar winds from OB associations becomes sufficiently high to excavate a cavity at the center of the starburst (McCray & Kafatos 1987). The collisions of multiple stellar winds and supernovae convert their kinetic energy into thermal energy, and, within the cavity, the hot gas reaches a sound speed much greater than the local escape velocity building a pressure that is much higher than the surrounding ISM. At high pressure gradients the outflow expands as a "super-bubble" along the path of strongest pressure gradient, sweeping up the ambient medium which collapses into a thin shell. The fate of the outflow, which may now be traveling at hundreds of kilometers per sec-

ond, depends on several factors (e.g. Heckman et al. 1990; Creasey et al. 2013). If the energy injection from stellar winds and supernovae falls, the expanding shell loses pressure, cools and eventually stops expanding. If the starburst is long lived ($>10^8$ yr), then the continual injection of energy results in a shell that continually expands, although dynamical and / or thermal processes may cause the shell to break up into clumps which allows the interior to freely expand and "blow out" of the galaxy (the so-called "superwind"). Since the superwind preferentially expands along the path of steepest pressure gradient, the outflows are expected to expand out of the plane of the galaxy, as seen in local starbursts (Lehnert & Heckman 1996).

The energetics associated with this "feedback" process are critically important for galaxy formation models. In cosmological simulations which do not include this stellar feedback, gas rapidly cools, producing high star-formation rates and the resulting stellar masses are approximately an order

of magnitude higher than observed (e.g. Somerville & Primack 1999; Cole et al. 2000; Benson et al. 2003; Kereš et al. 2009; Bower et al. 2012). Since the cold gas fraction in local galaxies is $\lesssim 5\%$ (Saintonge et al. 2011), reducing the star-formation efficiency does not solve the problem, especially in low mass galaxies (White & Frenk 1991). Moreover, the identification of metals within the lowest density regions of the inter-galactic medium from QSO absorption line studies (Meyer & York 1987; Simcoe et al. 2004) implies that baryons can not simply be prevented from entering halos, but rather that some energetic process must expel baryons from galaxies.

The physical origin and launching mechanism of such a process is usually attributed to energy and momentum input from supernovae and / or radiation pressure from massive stars (Murray et al. 2005, 2010; Krumholz & Thompson 2013). Both cosmological and high-resolution "zoom" simulations have demonstrated that the injection of energy from supernovae in the form of kinetic outflows with constant velocity efficiently removes gas from galaxies, solving the over-cooling problem by regulating star formation, and enriching the inter-galactic medium (Springel & Hernquist 2003; Hopkins et al. 2012; Creasey et al. 2013).

Observations of local dwarf starbursts and luminous infrared galaxies (LIRGs) also suggest that the properties of the outflows scale with those of the parent galaxies (Lehnert & Heckman 1996; Rupke et al. 2002; Martin 2005; Westmoquette et al. 2012): galaxies with higher stellar masses and star-formation rates tend to drive higher velocity outflows, in broad agreement with the momentum-driven wind model (Murray et al. 2005). In this model, radiation from massive stars is absorbed by dust which then couples to the gas resulting in galactic outflows in which the mass loading in the wind scales proportionally with the star-formation rate (Hopkins et al. 2012).

At high redshift, observations suggest that most star-forming galaxies are surrounded by "superwinds" (Pettini et al. 2002; Erb et al. 2006; Steidel et al. 2010; Alexander et al. 2010; Genzel et al. 2011; Newman et al. 2012a; Martin et al. 2012). Most of the evidence for these outflows comes from the comparison of nebular emission line velocities to the absorption lines velocities in the ISM. Velocity offsets and broad line widths of several hundred $\mathrm{km\,s^{-1}}$ have been measured, suggesting the outflows are large-scale (e.g. Steidel et al. 2010; Freeman et al. 2017; Förster Schreiber et al. 2018). Evidence for outflows associated with individual star-forming regions within high-redshift galaxies also exist (Newman et al. 2012b; Genzel et al. 2011, 2014), most likely locating the source of the outflows seen on large scales. However, to determine the mass outflow rate and kinetic energy in the wind and so provide the empirical constraints required to test theoretical models, the spatial geometry of the outflow must be constrained. To date, most of the high-redshift galaxies where the winds have been resolved are "clumpy disks" with high star-formation rates, but the ubiquity of winds in the Lyman-break galaxy study of Steidel et al. (2010) suggest they are not restricted to galaxies with clumpy morphologies.

To address some of these questions, in this paper, we exploit KMOS observations of the Hα emission in 743 star-forming galaxies at $z \sim 1$ which were taken as part of the KMOS Redshift One Spectroscopic Survey (KROSS).

The primary goal of the survey is to measure the spatially resolved dynamics, velocity dispersion and metallicities of main-sequence galaxies at $z \sim 1$ (Stott et al. 2016; Harrison et al. 2017). Here, we measure the energetics of starburst driven outflows using the luminosity, line width and spatial extent of the underlying Hα broad line(s) from these galaxies to measure the ubiquity, kinetic energy and coupling efficiency of the outflows to the radiation pressure and supernovae.

Throughout the paper, we use a ΛCDM cosmology (Spergel et al. 2007) with $\Omega_\Lambda = 0.73$, $\Omega_m = 0.27$, and $H_0 = 72\,\mathrm{km\,s^{-1}\,Mpc^{-1}}$ and adopt a Chabrier stellar initial mass function (IMF) (Chabrier 2003). In this cosmology, at $z = 0.90$ (the median redshift of the galaxies used in this paper), $1''$ corresponds to a physical scale of 7.8 kpc. All quoted magnitudes are on the AB system.

2 ANALYSIS & RESULTS

In this work, we examine galaxies observed as part of the KROSS. The sample selection, survey design and data reduction are described in detail in Stott et al. (2016) whilst the dynamical properties and final sample are described in detail in Harrison et al. (2017). Briefly, our KMOS sample comprises observations of 743 star-forming galaxies at $z \sim 1$ selected from some of the best studies extra-galactic survey fields (ECDFS, COSMOS, UDS and SSA 22). In the following analysis, we will stack the spectra of the galaxies in our sample to search for broad, underlying emission lines. Before stacking, we remove the large scale velocity gradients from the galaxy before creating the galaxy-integrated one-dimensional spectra. We therefore limit our analysis to those galaxies that are spatially resolved in Hα emission (although we note that if we include the unresolved galaxies in the following analysis – albeit without first removing the internal velocity gradients from their collapsed spectra – none of the quantitative conclusions are significantly changed). It is clearly fairer to omit these from the sample so that any broad line properties are not the result of strong beam-smearing effects. From our parent sample of 743 galaxies, 552 are spatially resolved in Hα (see Harrison et al. 2017 for details).

2.1 Removing (candidate) AGNs from the sample

In the following analysis, we search for (underlying) broad Hα (and [N II] and [S II]) emission from star-formation driven winds - a signature of out-flowing gas. Since these lines may be weak, we stack the spectra of the galaxies. However, any AGN in our sample could potentially contaminate the (broad) Hα and so next we identify (and remove) any galaxies with AGN signatures. The outflow signatures from AGN-dominated galaxies are discussed in Harrison et al. (2016) and Harrison et al. (in prep).

First, we remove 23 AGNs (from the 552 galaxies which are spatially resolved in Hα) flagged by Harrison et al. (2017), which are identified from a [N II] / Hα emission-line ratio of [N II] / H$\alpha > 0.8$ and / or a $> 1000\,\mathrm{km\,s^{-1}}$ Hα broad line component in the individual galaxy integrated spectra. We verify there are no remaining AGN by investigating the

Table 1. Properties of the narrow and broad lines

Stack	N_{gal}	$<SFR>$ ($M_\odot$ yr^{-1})	$<M_\star>$ (10^{10} M$_\odot$)	Narrow Component FWHM (km s^{-1})	$\frac{[\text{N\,II}]}{\text{H}\alpha}$	Broad Component $L_{\text{H}\alpha}$ (10^{41} erg s^{-1})	FWHM (km s^{-1})	$\frac{[\text{N\,II}]}{\text{H}\alpha}$	Δ(BIC)	σ(P$_f$)
All	529	6.7 ± 0.2	1.0 ± 0.1	119 ± 2	0.2 ± 0.1	2.8 ± 0.2	280 ± 3	0.3 ± 0.1	2947	32
SFR-1	89	2.4 ± 0.1	0.8 ± 0.1	104 ± 2	0.2 ± 0.1	1.4 ± 0.1	181 ± 3	0.1 ± 0.1	35	5
SFR-2	108	4.3 ± 0.1	0.8 ± 0.1	122 ± 4	0.2 ± 0.1	1.9 ± 0.4	202 ± 5	0.3 ± 0.1	208	13
SFR-3	110	6.4 ± 0.1	1.0 ± 0.1	116 ± 2	0.1 ± 0.1	2.6 ± 0.3	231 ± 4	0.3 ± 0.1	696	22
SFR-4	111	9.2 ± 0.1	1.1 ± 0.1	130 ± 2	0.2 ± 0.1	2.8 ± 0.3	247 ± 5	0.4 ± 0.1	686	23
SFR-5	111	16.2 ± 0.8	1.5 ± 0.2	135 ± 2	0.2 ± 0.1	4.9 ± 0.3	277 ± 4	0.3 ± 0.1	1346	28
Mass-1	100	4.8 ± 0.6	0.2 ± 0.1	120 ± 4	0.1 ± 0.1	1.1 ± 0.3	180 ± 8	0.0 ± 0.1	149	9
Mass-2	124	6.4 ± 0.4	0.6 ± 0.1	107 ± 3	0.2 ± 0.1	3.5 ± 0.5	197 ± 4	0.2 ± 0.1	533	19
Mass-3	124	7.1 ± 0.7	1.1 ± 0.1	119 ± 2	0.2 ± 0.1	4.1 ± 0.1	212 ± 3	0.3 ± 0.1	293	14
Mass-4	99	7.8 ± 0.8	2.0 ± 0.1	133 ± 2	0.2 ± 0.1	3.1 ± 0.2	277 ± 5	0.5 ± 0.1	1344	24
Mass-5	82	8.0 ± 0.7	4.0 ± 0.1	140 ± 2	0.2 ± 0.1	2.5 ± 0.2	323 ± 6	0.6 ± 0.2	2096	25
SFRD-1[0.0–0.02]	95	3.1 ± 0.2	0.8 ± 0.1	118 ± 6	0.2 ± 0.1	1.2 ± 0.4	203 ± 10	0.2 ± 0.1	112	8
SFRD-2[0.02–0.05]	103	4.3 ± 0.2	1.1 ± 0.1	112 ± 2	0.2 ± 0.1	2.5 ± 0.1	207 ± 3	0.3 ± 0.1	196	13
SFRD-3[0.05–0.09]	109	5.9 ± 0.3	0.9 ± 0.1	121 ± 4	0.2 ± 0.1	2.8 ± 0.5	210 ± 5	0.3 ± 0.1	271	15
SFRD-4[0.09–0.16]	111	8.0 ± 0.2	1.0 ± 0.1	119 ± 2	0.1 ± 0.1	2.6 ± 0.2	246 ± 4	0.4 ± 0.1	1067	28
SFRD-5[0.16–1.02]	111	14.7 ± 0.6	1.3 ± 0.1	135 ± 2	0.2 ± 0.1	5.1 ± 0.3	268 ± 4	0.3 ± 0.1	1074	25
i-1[0–36]	110	6.3 ± 0.5	1.2 ± 0.2	106 ± 3	0.2 ± 0.1	3.3 ± 0.4	208 ± 4	0.3 ± 0.1	736	21
i-2[36–46]	106	8.5 ± 0.8	1.2 ± 0.1	122 ± 3	0.1 ± 0.1	3.2 ± 0.4	232 ± 5	0.4 ± 0.2	784	21
i-3[46–54]	106	6.0 ± 0.4	0.7 ± 0.1	124 ± 3	0.1 ± 0.1	2.0 ± 0.2	235 ± 6	0.3 ± 0.1	618	17
i-4[54–65]	103	7.3 ± 0.5	1.1 ± 0.1	129 ± 3	0.1 ± 0.1	2.6 ± 0.3	245 ± 6	0.3 ± 0.1	693	19
i-5[65–90]	104	5.8 ± 0.4	0.9 ± 0.1	121 ± 4	0.1 ± 0.1	3.0 ± 0.5	222 ± 5	0.3 ± 0.1	390	14
sSFR-1[0.06–2.4]	92	3.8 ± 0.3	3.0 ± 0.2	132 ± 3	0.2 ± 0.1	1.2 ± 0.1	279 ± 7	0.5 ± 0.2	556	18
sSFR-2[2.4–4.9]	106	6.1 ± 0.3	1.8 ± 0.1	124 ± 2	0.2 ± 0.1	2.6 ± 0.2	259 ± 4	0.5 ± 0.1	743	22
sSFR-3[4.9–8.8]	110	7.0 ± 0.5	1.0 ± 0.1	112 ± 2	0.2 ± 0.1	4.1 ± 0.0	217 ± 3	0.3 ± 0.1	519	19
sSFR-4[8.8–16]	111	7.6 ± 0.6	0.6 ± 0.1	124 ± 3	0.1 ± 0.1	3.0 ± 0.5	206 ± 4	0.3 ± 0.1	309	15
sSFR-5[1.6–210]	110	9.7 ± 0.6	0.4 ± 0.1	122 ± 2	0.1 ± 0.1	2.3 ± 0.3	214 ± 6	0.1 ± 0.1	425	17

Notes: [N II] / Hα denotes [N II]$\lambda6583$ / Hα flux ratio. σ(P$_f$) denotes the f-test significance of the improvement of a narrow + broad line fit over a narrow-only fit. The units of the ranges in column 1 for the star formation rate density (SFRD); inclination (i) and specific star formation rate (sSFR) are $M_\odot$ / kpc^2; degrees and 10^{-10} yr^{-1} respectively.

X-ray luminosities. We cross correlated the remaining sample with the *Chandra* X-ray catalogs for their respective fields. Six of the galaxies in our remaining sample have X-ray counterparts, all in the CDFS region and detected in the 2 Ms catalog of Luo et al. (2008). However, the 2–10 keV fluxes of these galaxies, $f_X = 2$–3×10^{-17} erg s^{-1} cm^{-2} correspond to luminosities of $L_X = 0.5$–1.5×10^{41} erg s^{-1}, which is a factor ~ 10 below the canonical luminosity expected for the classification of a source as an AGN ($L_X \sim 10^{42}$ erg s^{-1}). Since the X-ray emission can be heavily obscured, finally, we search for obscured AGNs using the mid-infrared emission (e.g. Stern et al. 2005) using the 5.8–$3.6\,\mu$m versus 8.0–$4.5\,\mu$m IRAC colours which can identify galaxies which are strong power-law sources at these redshifts (e.g. Donley et al. 2012). However, no additional candidate AGNs are identified.

Omitting any candidate AGNs and unresolved galaxies from the sample leaves 529 galaxies for our analysis with well resolved dynamics. The median redshift for this sample is $z = 0.85^{+0.05}_{-0.03}$ and the median stellar mass is $\log(M_\star / M_\odot) = 10.0 \pm 0.4$ with a quartile range of $\log(M_\star / M_\odot) = 9.5$–$10.6$.

2.2 Composite Spectra

Before creating composite spectra, we must remove the large scale velocity gradients from the galaxy kinematics which will otherwise artificially broaden the observed line emission in the collapsed, one-dimensional spectrum of each galaxy (e.g. for a disk-like system, we need to remove the galaxy's rotation from the cube; e.g. see Harrison et al. 2017). To achieve this, we shift the spectra in each pixel to the rest-frame (based on the redshift of the Hα at that pixel) to create a 'velocity-subtracted' datacube. To highlight the effects of this procedure, in Fig. 1 we show the position-velocity diagram and collapsed, one-dimensional spectrum for one of the galaxies in our sample before and after the galaxy dynamics have been removed from the cube. In this figure, both of the the position-velocity diagrams are extracted along the same major kinematic axis of the galaxy. Before the large scale dynamics have been subtracted, the rotation of the disk can be seen clearly, with a peak-to-peak velocity gradient of 260 ± 10 km s^{-1} across $\sim 2''$ in projection. The position-velocity diagram extracted from the same kinematic axis of the 'velocity-subtracted' cube however shows no velocity gradient, demonstrating that the large scale dynamics have been removed. We also show the collapsed, one-dimensional spectrum for both cubes, integrated over the same pixels. This demonstrates that removing the large-scale dynamics from the galaxy reduces the line width of the Hα, from $\sigma = 227 \pm 11$ km s^{-1} extracted from the original cube to $\sigma = 119 \pm 9$ km s^{-1} in the velocity-subtracted cube.

We caution that it is possible that there may be galaxies in our sample where the extended Hα emission is dominated by an outflow (e.g. a biconical outflow arising from a compact galaxy). In this case, removing the velocity gradients
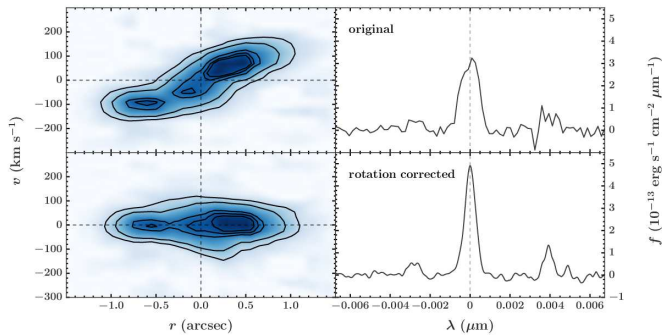
Figure 1. Position-velocity diagrams (*Left*) and collapsed, one-dimensional spectra (*Right*) for one of the galaxies in our sample. The top and bottom row shows the position-velocity diagram and one-dimensional spectra from the datacube respectively before- and after- the large-scale dynamics have been removed. The position-velocity diagrams are extracted from the same major kinematic axis of the galaxy, and the one-dimensional spectra are extracted from the same pixels in both cubes. This demonstrates how removing the large scale galaxy dynamics reduces the line width of the galaxy-integrated $H\alpha$ emission. In this case, the width of the $H\alpha$ is reduced from $\sigma = 227 \pm 11\,\mathrm{km\,s^{-1}}$ to $\sigma = 119 \pm 9\,\mathrm{km\,s^{-1}}$ in the velocity-subtracted cube.

will artificially narrow the broad-line(s) we are searching for. To test whether this may be the case, we compare the major kinematic axis (defined from $H\alpha$) to the major morphological axis (defined from *I*- or *H*-band *HST* or ground-based *K*-band imaging). The median offset between these two position angles is $\Delta(|\mathrm{PA}|) = 13 \pm 10°$ (see also Harrison et al. 2017)). Thus it appears that the major kinematic axis and major morphological axis are typically well aligned, which suggests strong systematic effects from biconical outflows aligned perpendicular to the disk do not dominate the $H\alpha$ kinematics.

To create a one-dimensional spectrum for each galaxy, we collapse the velocity-subtracted datacube cube over $H\alpha$ region defined by the pixel-to-pixel fitting (which reach a median surface brightness limit of $7 \times 10^{-19}\,\mathrm{erg\,s^{-1}\,cm^{-2}\,arcsec^{-2}}$). We then continuum subtract the galaxy spectrum using line free regions of continuum (defined by regions at least $10\,000\,\mathrm{km\,s^{-1}}$ from any emission lines) and normalise each galaxy-integrated spectrum by its $H\alpha$ luminosity to ensure the brightest galaxies do not dominate the stacks. A stacked spectrum is created by using a sigma-clipped average (using 3σ clipping at each wavelength). However, we note that all of the results in the following sections are insensitive to using a sigma clipped average, inverse sky-weighted mean, median or bootstrap average.

In Fig. 2 we show the composite spectrum for all of the galaxies in our sample. In this stack, we make strong detections of the $H\alpha$, [NII] and [SII] doublets, HeI $\lambda 5876$, OI $\lambda 6300$ emission lines and weak NaD $\lambda 5892$ absorption. We note that the effective integration time in this stack is $\sim 3000\,\mathrm{hrs}$ for a galaxy with an average star formation rate of $\mathrm{SFR} \sim 9\,\mathrm{M_\odot\,yr^{-1}}$ and stellar mass of $\mathrm{M_\star} \sim 10^{10}\,\mathrm{M_\odot}$.

2.3 Searching for Underlying Broad Lines and Gas Outflows

To search for a broad, underlying emission in the composite spectrum, we use the MPFIT routine to first fit the narrow-lines of the $H\alpha$, [NII] and [SII] doublets (allowing the line widths and normalisations to vary but fixing the [NII] emission line ratio at $[\mathrm{NII}]\lambda 6583\,/\,[\mathrm{NII}]\lambda 6543 = 2.95$; Osterbrock & Shuder 1982). We then attempt a second fit that includes a broad, underlying emission component in the [NII], $H\alpha$ and [SII] lines. When fitting a broad component, we couple the broad line FWHM and velocity centroid of the underlying [NII], $H\alpha$ and [SII]. In Fig. 2 we show the best narrow + broad-line fit to the composite spectra. We also show the residual spectra for the narrow-only and narrow+broad line fits. This demonstrates that the narrow-line only fit provides a poor fit to the data compared to the narrow+broad line profile.

To quantify the improved significance of the broad+narrow line fit compared to the narrow line-only fit, we perform two tests. First, we use the BIC statistic; $\Delta\,\mathrm{BIC} = (\chi_1^2 + k_1 ln(n)) - (\chi_2^2 + k_2 ln(n))$ where $\chi_{1,2}^2$ are the total χ^2 of the line fit from the narrow- and narrow + broad models, $k_{1,2}$ are the number of degrees of free parameters in the fit and n is the number of data points. We adopt $\Delta\,\mathrm{BIC} > 10$ as strong evidence that a broad line component is required. We also perform an f-test between the two fits, with $f = (\chi_1^2 - \chi_2^2)\,/\,(N_{\mathrm{dof},1} - N_{\mathrm{dof},2})\,/\,(\chi_2^2\,/\,N_{\mathrm{dof},2})$ and compute the significance of the improvement using the probability assuming a normal distribution. We report both values in Table 1. In all of the following sections, we only report the properties of the broad-lines if the broad + narrow-line fit provides a significant improvement over the narrow-only line fit at > 5-σ significance.

Since broad, underlying emission could also conceivably be mimicked from gas motions obeying a Lorentzian distribution, we also attempt a Lorentzian fit to the stack. In this fit, we fix the wavelength of the $H\alpha$ and the doublets of [NII] and [SII], but allow their width and normalisation to vary (fixing the ratio of $[\mathrm{NII}]\lambda 6583\,/\,[\mathrm{NII}]6543 = 2.95$). However, the best-fit Lorentzian profile provides a significantly poorer (> 7-σ) description of the data in every case. We therefore adopt Gaussian profiles as our preferred method of describing the narrow / broad components in all of the following sections.

Finally, we note that we have not attempted to correct the spectra for Balmer absorption lines in the composite spectra. However, to test what effect this might have, we generate synthetic stellar spectra using the updated Bruzual-Charlot stellar population libraries (Bruzual & Charlot 2003). We generate a grid of spectra for a range of star-formation histories (constant and exponential star formation rates with e-folding times of $\tau = 0.25\ 0.5$, 1, 2, 5-Gyr) observed at ages that range from $10\,\mathrm{Myr}$ to $8\,\mathrm{Gyr}$ (with 100 steps that are log-spaced in time) with metallicities ranging from 0.01 to $2\,\mathrm{Z_\odot}$. From each spectrum, we measure the equivalent width of the $H\alpha$, which has a range of $\mathrm{W_{0,H\alpha}} = -1.5$ to $-5.5\,\text{Å}$ with a median of $\mathrm{W_{0,H\alpha}} = -4.0 \pm 0.5\,\text{Å}$. This is much smaller than the median equivalent width of the narrow-line $H\alpha$ emission in an individual galaxy (or stack), which has $\mathrm{W_{0,H\alpha}} = 25\text{Å}$. Since the equivalent width of the $H\alpha$ emission is stronger than
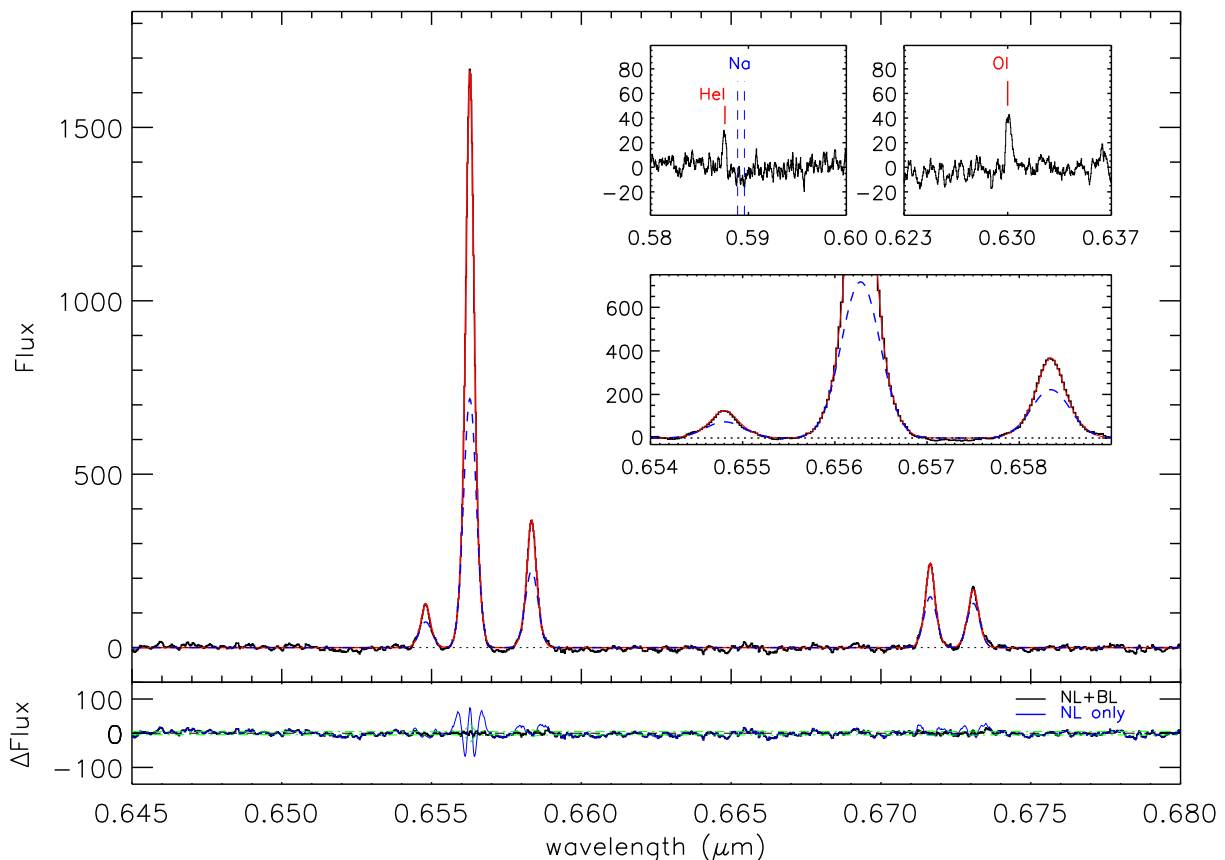
Figure 2. Rest-frame optical composite of 529 $z \sim 1$ star-forming galaxies from our KMOS observations (black). We overlay the best fit model (red) which comprises both narrow- and broad- emission line components (the broad-line component is overlaid as blue dashed, and zoomed-up in the central inset). The upper inset shows the detection of the HeI $\lambda 5876$ and OI $\lambda 6300$ emission, as well as the NaD $\lambda\lambda 5896, 5889$ absorption line doublet. We clearly detect strong, broad underlying emission which is evident in the Hα, [NII] and [SII], with FWHM $= 280 \pm 3$ km s^{-1}. The identification of broad emission is suggestive of outflowing material, and since the broad emission is seen in the forbidden lines, this suggests that the outflow must arise from the ISM (rather than any hidden AGN broad-line region). The lower panel shows the residuals from the best-fit (data - model) for a narrow-emission line fit only (blue) and broad+narrow emission line fit (black), which demonstrates that the inclusion of the broad component significantly improves the fit.

that of the absorption, we have not attempted to correct for it here.

2.4 Properties of the Composite Spectra

The inclusion of the broad, underlying component in addition to the single narrow Gaussian profile in the stacked spectra in Fig. 2 provides a significant ($\sim 32\,\sigma$) improvement over a single Gaussian profile-only fit. The broad Hα has a FWHM $= 280 \pm 3$ km s^{-1} (more than twice that of the narrow-line Hα, FWHM $= 119 \pm 2$ km s^{-1}). The narrow-line Hα FWHM is similar to the typical gas-phase velocity dispersion for a high-redshift disk; (e.g. Lehnert et al. 2013; Wisnioski et al. 2015; Johnson et al. 2018; Turner et al. 2017). Crucially, the broad emission is not only seen in the Hα, but also clearly seen in the forbidden lines of [NII] and [SII]. Whilst broad Hα is often associated with the broad-line region of an AGN, the identification of similarly broad forbidden lines within the spectrum suggest that the broad emission originates in the lower-density ISM.

To test whether the broad line emission arises only in the nuclear regions, we create a stack for all pixels which are located $> 0.7''$ (i.e. outside of 5 kpc and larger

than the seeing disk) from the galaxy center, and another with all pixels within $0.7''$ of the dynamical center. In both spectra we identify broad, underlying emission with FWHM $= 308 \pm 6$ km s^{-1} and FWHM $= 286 \pm 7$ km s^{-1} for the $r < 0.7''$ and $r > 0.7''$ apertures respectively. This suggests that the broad, underlying emission is not confined to the nuclear regions, but is a galaxy-wide phenomenon (we discuss this further in Section 2.5).

As Fig. 2 shows, the composite spectrum shows strong [NII], Hα and [SII] emission, but we also detect the HeI $\lambda 5876$ and (low ionisation) OI $\lambda 6300$ emission lines with ratios of OI / H$\alpha = 0.036 \pm 0.003$ and HeI / H$\alpha = 0.020 \pm 0.002$ (in these calculations we use the total Hα emission line flux since there is insufficient signal-to-noise to decompose the HeI and [OI] in to narrow and broad components). The [OI] / Hα emission line ratio provides a diagnostic of the average ISM conditions. The [OI] / Hα emission line ratio is relatively weak in gas photo-ionised by stars ([OI] / H$\alpha \lesssim 0.08$) and stronger in shock-heated gas and AGN (Osterbrock 1989; Kewley et al. 2006). Indeed, in the classification system of Kewley et al. (2006), "transition" (or composite) galaxies and AGN are classified by OI / H$\alpha \gtrsim 0.06$ and 0.15 respectively with all galaxies with OI / H$\alpha \lesssim 0.05$ classed as HII

region-like (this is also the case if we use the total [OI] flux and narrow Hα flux). Thus, the line ratios suggest that the ionisation of the ISM in our sample is dominated by photoionisation of the gas.

An important quantity for measuring the ionised gas mass and hence mass outflow rates is the electron density (n_e). This quantity is often measured from the ratio of the [SII] $\lambda6716,6731$ doublet. The forbidden lines of [SII] $\lambda6716,6731$ arise in low-density gas, where there are too few collisions to de-excite the excited state. In the low density regime ($\lesssim 10\,\mathrm{cm}^{-3}$), the ratio of the [SII]$\lambda6716$ / [SII]$\lambda6731$ provides a statistical weight, reflecting how many electrons the level can hold. At high density ($\gtrsim 10^4\,\mathrm{cm}^{-3}$), the ratio instead reflects the shorter lifetime of the $\lambda6731$Å transition. In between, the ratio measures the gas density (e.g. Osterbrock & Ferland 2006).

From the integrated spectra (Fig. 2), we measure a narrow-line ratio of [SII]$\lambda6716$ / [SII]$\lambda6731 = 1.4 \pm 0.1$, which implies an electron density of $n_\mathrm{e} = 30^{+40}_{-20}\,\mathrm{cm}^{-3}$, and a broad line ratio of [SII] 6716 / [SII]$\lambda6731 = 1.3 \pm 0.1$, which suggests an electron density of $n_\mathrm{e} = 75^{+55}_{-50}\,\mathrm{cm}^{-3}$ (Osterbrock & Ferland 2006).

2.5 Spatial Extent and Limits on the Geometry of the Outflows

Before we can use these data to estimate properties of the high velocity gas (such as the potential mass in the wind, the mass loading and its kinetic energy), we first require an estimate of the typical spatial extent and geometry of the outflows. We therefore stack the galaxy spectra in annulli (adopting the dynamical center from the best-fit disk model) and search for broad, underlying emission (Fig. 3). To account for differences in galaxies sizes in the sample, in Fig. 3 we parameterise the intensity and intensity ratio and FWHM of the broad Hα in terms of half-light radii of the galaxies. The spatial extent of the broad Hα emission appears to be extended over at least 2.5 half light radii (the median half light radius of the sample is 2.7 ± 0.1 kpc with a quartile range of 1.8–3.4 kpc). As a further test, we also bin all the spectra from the cubes ranked by their (normalised) radius (in top sets of 100 spectra) and then fit each of the stacks and measure the broad and narrow line intensity ratios and FWHM. We also overlay these results in Fig. 3, which show good agreement with the results from coarser bins, and suggests that the outflows are not confined to the central regions, but extend across several half-light radii.

Since some of the galaxies are small (and so normalising by half light radii may introduce artificial effects from the seeing), we also measure the spatial extent of the broad Hα in radial bins in arcseconds (without renormalising), and estimate a spatial FWHM of the broad-line intensity of $1.5 \pm 0.2''$ (10 kpc at $z = 1$). This corresponds to ~ 10 kpc at $z \sim 1$ further suggesting that the outflows are not confined to the nuclear regions. It is interesting to note that the FWHM of the broad line falls over the range 1–10 kpc (Fig. 3). This is similar to local starbursts, where the FWHM from the outflowing gas along the major axis of the galaxy falls rapidly with radius (e.g. Lehnert & Heckman 1996; although note that the disks studied in Lehnert & Heckman (1996) have half light radii which are a factor $\sim 2 \times$ larger than those studied here).
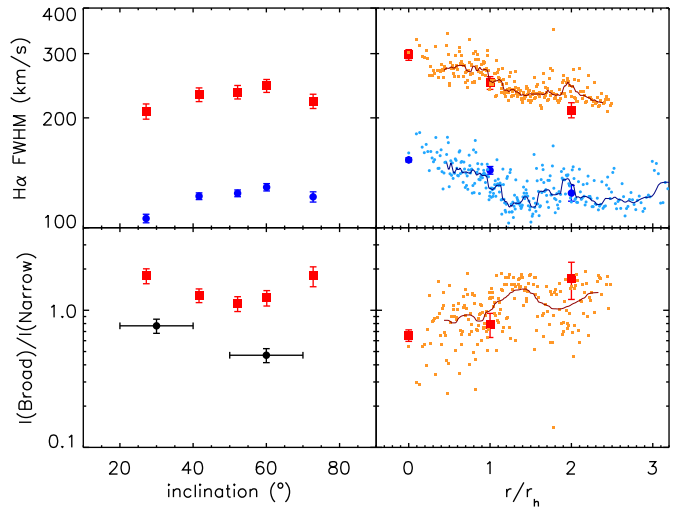
Figure 3. Hα broad- and narrow- line properties as a function of inclination and radius. *Top Left:* Hα FWHM for the narrow (circle) and broad (square) Gaussian profiles as a function of galaxy inclination. The data show a weak trend of increasing broad line FWHM with inclination, from 208 ± 4 km s^{-1} for galaxies at low inclination, to 245 ± 6 km s^{-1} for more highly inclined galaxies. Although the trend is weak, it is consistent with several other studies which have also shown that outflows tend to be bi-polar with wide opening angles (Martin et al. 2012; Bordoloi et al. 2011). *Top Right:* Hα FWHM for the broad and narrow Gaussian profile as a function of radius (normalised to half light radius). The large symbols show the FWHM in three radial bins, whilst the small points show the FWHM in bins that each contain 100 spectra from the datacubes, ranked by their (normalised) radius (in units of r / r_h). The solid lines denote running medians through the data. *Bottom Left:* Hα broad / narrow-line luminosity ratio as a function of inclination. The solid circles show the intensity ratio of broad-to-narrow line intensities from the SINS survey (Newman et al. 2012a). *Bottom Right:* Hα broad / narrow-line luminosity ratio as a function of radius (normalised to half light radius). The small points show the FWHM in bins that each contain 100 spectra from the cubes, with the solid line showing a running median through the data, demonstrating that the luminosity ratio of broad- to narrow-line Hα flux increases with half light radii.

In the KMOS sample, we also detect strong variation in the emission line ratios with increasing galacto-centric radius in the broad lines (Fig. 4), with $([\mathrm{NII}] / \mathrm{H}\alpha)_\mathrm{BL} = (-0.0253 \pm 0.004)\, r_\mathrm{kpc} + (0.47 \pm 0.02)$. In contrast, the gradient in the ratio of [NII] / Hα emission line intensities with galacto-centric radius is shallow, with $([\mathrm{NII}] / \mathrm{H}\alpha)_\mathrm{NL} = (-0.006 \pm 0.003)\, r_\mathrm{kpc} + (0.22 \pm 0.02)$ (Fig. 4). The gradient in [NII] / Hα with radius for the narrow-line emission is comparable to the negative, but shallow metallicity gradients seen in individual high-redshift galaxies (Yuan et al. 2011; Queyrel et al. 2012; Stott et al. 2014).

Considering instead the [SII] emission line, in the same radial bins we do not detect any significant variation in the narrow-line ratio of $\mathrm{S2} = I_{6716} / I_{6731}$, with an average of $\mathrm{S2} = 1.45 \pm 0.15$ (which is consistent with that derived from the composite). The emission line ratio of I_{6716} / I_{6731} for the broad component displays a weak trend with galacto-centric radius. However since the trend is only
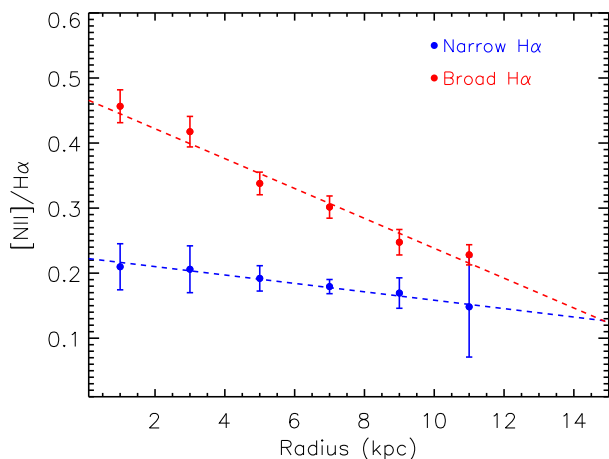
Figure 4. [N II] / Hα emission line profiles for the narrow- and broad- emission lines in the stacked spectra as a function of galacto-centric radius. Both the narrow- and broad- emission line ratios decline with increasing radius, although the narrow-line gradient is much weaker (but consistent with that typically detected in individual high-redshift galaxies).

2σ, (with $S2 \propto (-0.006 \pm 0.003)\, r_{\rm kpc}$), in all following sections we adopt a fixed emission line ratio for the I_{6716} / I_{6731} doublet, with $S2 = 1.4$ and $S2 = 1.3$ for the narrow- and broad- lines respectively.

Since the [O I] $\lambda 6300$Å line is weak compared to Hα we investigate the [O I] / Hα ratio only in the inner- versus outer-regions. The signal-to-noise of the [O I] precludes decomposing the [O I] into a broad and narrow component. However, in integrated properties, we find a similar trend as seen in the [N II] such that the central regions have a higher emission line flux ratio, with [O I] / Hα = (0.038 ± 0.003) compared to [O I] / Hα < 0.0031 in the outer regions. Thus, the [N II] / Hα, and [O I] / Hα gradients appear to reflect the increased ionisation of the outflow in the central regions.

A prediction of the superwind model is that there should be a strong pressure gradient (an approximately constant pressure profile within the ISM around the energy-injecting source and an outer region where the outflowing wind expands freely and the pressure falls off as $1/r^2$).

We convert this into a pressure assuming a constant temperature (10^4 K) and a total density three times that of the electron density determined from the [S II] ratio (to account for the fact that the [S II] lines are formed in the partially ionised zone of the nebulae). This suggests a pressure $P / k_{\rm B} = 1$–3×10^6 K cm^{-3} (100–300 × that of the mid-plane of the Milky-Way) which is approximately constant over the radius 1–10 kpc. This observation suggests that pressures much higher than in the Milky-Way are maintained over a large volume (up to several kpc^3) in the centers of these galaxies. If the pressure does decrease with radius in the regime where the winds expand freely, this must occur on scales >10 kpc.

Since outflows should expand preferentially along the path of the steepest pressure gradient, they are expected to preferentially expand out of the plane of the galaxy (Lehnert & Heckman 1996). In local galaxies, the winds tend to be weakly collimated (e.g. Dahlem et al. 1997; Chen et al. 2010; Bordoloi et al. 2011). To search for the same

effect in our KMOS sample, and so test whether the winds are collimated, or whether they are spherically symmetric (or wide angle), we split the sample into five bins of inclination, each bin containing the same number of galaxies, and measure the FWHM of the broad and narrow components. We identify broad Hα in all cases, with FWHM ranging from 208 ± 4 km / s^{-1} for galaxies at low inclination, to 245 ± 6 km s^{-1} for more highly inclined galaxies (Fig. 3). Although the trend is only weak, it is consistent with several other studies which have also shown that outflows tend to be bi-polar with wide opening angles (Martin et al. 2012; Bordoloi et al. 2011).

3 DISCUSSION

With broad lines identified in the galaxy spectra, we can use the broad line intensity and width to estimate the energetics of the outflowing gas.

3.1 Outflow Scaling Relations

Before estimating the mass outflow rates and kinetic energy in the wind from the composite stack, we first investigate the dependence of broad-line Hα properties with galaxy properties. We reiterate that there are significant systematic uncertainties in the absolute scaling of the mass outflow rates, kinetic energy and coupling efficiency we have derived. However the relative scaling (e.g. with mass or star formation rate) should be much more reliable. The most straight-forward prediction of the superwind theory is that the properties of the emission-line gas should be related to the star-formation rate of the galaxies since the "roots" of the outflows are located in the OB associations and associated supernovae events. Other properties, such as rotation speed and axial ratio are expected to correlate more weakly. For example, Hopkins et al. (2012) predict that the mass outflow rate from starburst-driven superwinds scales linearly with star-formation rate. Indeed, Martin et al. (2012) used low-ionisation absorption lines to show that the velocity of the out-flowing gas scales with star-formation rate in galaxies at $z = 0.4$–1.4, whilst Genzel et al. (2014) used a sample of high-redshift, massive, star-forming galaxies and AGNs to suggests that the outflow velocity scales with galaxy mass and star-formation rate.

To investigate how the outflow properties depend on the global galaxy properties in our sample, we divide the sample into five bins of mass and five bins of star-formation rate (with equal numbers of galaxies in each bin) and show the resulting spectral stacks in Fig. 5. Since sub-dividing the sample reduces the signal-to-noise, we fix the velocity offset between the narrow- and broad- components for all line to zero (although we note that a free fit returns velocity offsets <10 km s^{-1} in all cases). We also fix the ratios of the broad- emission line intensities of the [S II] doublet to their average values from the stack of all galaxies (§ 2.5), but continue to allow variation in the relative contribution of the broad/narrow lines. In all of the following sections, the quoted errors on the line ratios and/or velocity widths incorporate the covariance between the fitted parameters. As the spectra in Fig. 5 show, there appears to
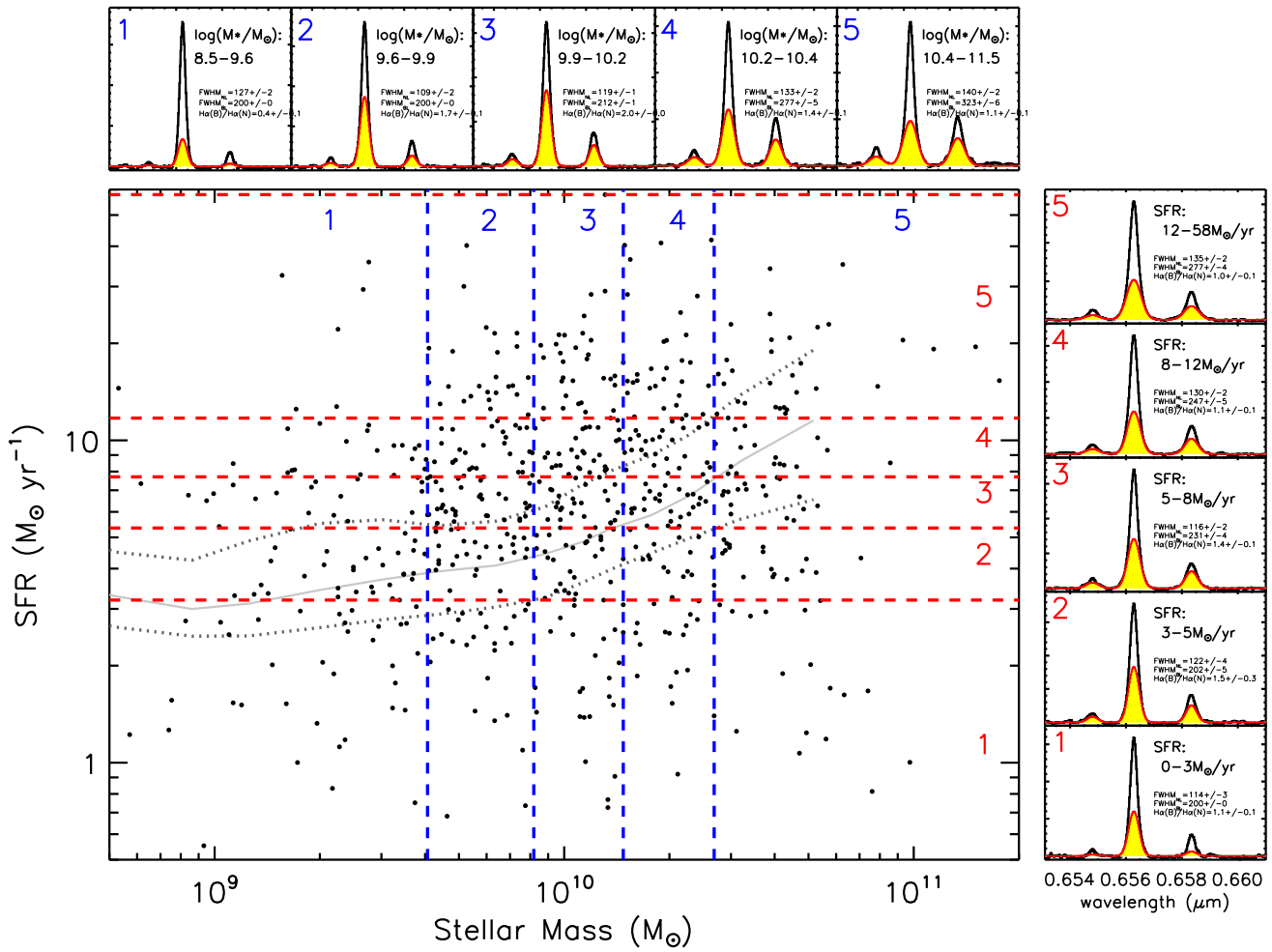
Figure 5. Stacked spectra for the galaxies in our sample as a function of stellar mass and star formation rate. The main panel shows the stellar masses and star formation rates for the sample. We bin the sample in to 5 bins of stellar mass and star formation rate (labeled 1–5 in each case). Each bin contains the same number of galaxies, and are shown by the dashed lines. The panels across the top and right-hand side of the figure show the stacked spectra for each bin, including the underlying broad line emission. These plots demonstrate that the broad, underlying emission increases in FWHM with increasing stellar mass and star-formation rate.

be a trend of increasing broad-line Hα FWHM and intensity with both mass and star formation rate, which is also shown in Fig. 6. In the local Universe, the velocity of outflowing gas has also been shown to correlate with star-formation rate, with a factor ~ 30 change in velocity observed over a range of four orders of magnitude of SFR ($v_{\rm wind} \propto {\rm SFR}^{0.3}$; Rupke et al. 2005; Martin 2005). Indeed, this figure shows that the high-redshift galaxies in our sample also tend to have broader lines with increasing star-formation rate (increasing from FWHM $\sim 180 \, {\rm km \, s^{-1}}$ to $350 \, {\rm km \, s^{-1}}$ between SFR $= 1$–$2 \, {\rm M_\odot \, yr^{-1}}$ to $\gtrsim 30 \, {\rm M_\odot \, yr^{-1}}$) and mass (increasing from FWHM $\sim 180 \, {\rm km \, s^{-1}}$ to $323 \, {\rm km \, s^{-1}}$ between $M_\star \sim (0.2$–$4) \times 10^{10} \, {\rm M_\odot}$). Although we do not have the same dynamic range in star-formation rate as the local samples, a power-law fit to the broad-line Hα velocities in Fig. 6 yields FWHM $\propto {\rm SFR}^{0.24 \pm 0.08}$ and FWHM $\propto M_\star^{0.29 \pm 0.08}$.

In Fig. 6 we also plot the FWHM and broad / narrow line intensity ratio of the underlying broad-line Hα with star formation surface density. We plot the galaxy-averaged values, but we also rank the pixels in each datacube by their individual star formation surface density and then calculate

the broad-line FWHM using bins that each contain 100 spectra. Both the galaxy-averaged and pixel-to-pixel values show show a strong trend in broad line FWHM that increases strongly with increasing star formation surface density.

Similar trends of increasing broad-line widths with star-formation rate have also been seen in the stacked Hα spectra of $z = 1$–2 galaxies from Newman et al. (2012a) and Genzel et al. (2014) as well as in $z \sim 1$ star-forming galaxies selected from the DEEP2 survey (Martin et al. 2012). We note that the velocities measured in the rest-frame UV / optical spectra from Martin et al. (2012) use low ionisation lines (such as FeII and MgII), measuring the maximum velocity, $v_{\rm max}$ as the velocity at which the absorption line depth plus 1-σ noise is consistent with the continuum. To compare this value to our FWHM, we construct a set of model spectra with an absorption line doublet of variable FWHM and intensity appropriate for the DEEP2 sample and add noise such that the signal-to-noise per pixel is 5–7σ (similar to the data in Martin et al. 2012). For a reasonable range in FWHM and S / N, we estimate FWHM $= 1.6 \, v_{\rm max}$ and use
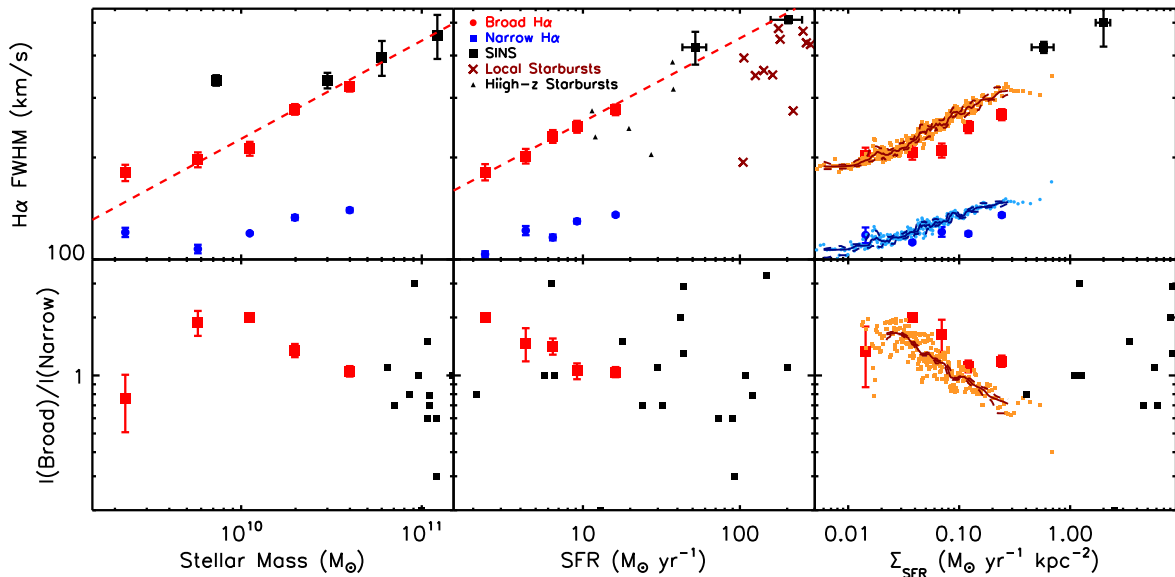
Figure 6. Physical properties of the Hα broad lines as a function of mass, star formation rate and star formation surface density for the galaxies in our sample. *Top Left:* Line width versus stellar mass for the galaxies in our sample compared to the SINS+KMOS^{3D} survey of broad Hα in $z = 1$–2 galaxies from Newman et al. (2012a) and Genzel et al. (2014) and DEEP2 galaxies from Martin et al. (2012). The dashed line shows the outflow velocity as a function of mass with FWHM $\propto$ M$_\star^{0.29}$. *Top Center:* Hα line width (FWHM) as a function of star formation rate. The more actively star-forming galaxies tend to higher broad-line widths, increasing from FWHM $\sim 180\,\mathrm{km\,s^{-1}}$ to $350\,\mathrm{km\,s^{-1}}$ between SFR $= 1$–$2\,\mathrm{M_\odot\,yr^{-1}}$ to $\gtrsim 30\,\mathrm{M_\odot\,yr^{-1}}$. We also plot the variation in narrow-line Hα FWHM. Similar trends of increasing broad-line widths with star-formation rate have also been seen in Hα (e.g. Newman et al. 2012a; Genzel et al. 2014) and in low ionisation lines (Martin et al. 2012). The dashed line shows a power-law fit to the broad-line Hα velocities in with FWHM $\propto$ SFR$^{0.24}$. *Top Right:* Broad line Hα FWHM as a function of star formation surface density. The large points denote the galaxy-averaged values, which show an increasing broad line FWHM with increasing star formation surface density. We rank the pixels in each datacube by their individual star formation surface densities and plot the broad-line FWHM using bins that each contain 100 spectra (small points). The red dashed solid line shows the running median through those data (with dashed lines denoting the central 68% of the distribution). In this plot, both the galaxy-averaged and pixel-to-pixel values show show a strong trend in broad line FWHM that increases strongly with increasing star formation surface density. *Lower Left:* Broad Hα emission line flux fraction ($f_{\mathrm{broad}}\,/\,f_{\mathrm{narrow}}$) as a function of stellar mass. The broad Hα fraction is high, with $f_{\mathrm{broad}}\,/\,f_{\mathrm{narrow}} = 1$–2 across a decade of stellar masses. *Lower Middle:* Broad Hα fraction as a function of star formation rate, which shows a similarly strong broad / narrow emission line flux ratio. *Lower Right:* Broad / Narrow Hα emission line flux ratio as a function of star formation surface density. We plot the galaxy average values (large solid points), and also the measurements from the ranked pixels from each datacube, with each measurement derived from 100 spectra. The red dashed solid line shows the running median through those data (with dashed lines denoting the central 68% of the distribution).

this conversion when comparing results from Martin et al. (2012) in Fig. 6.

In Fig. 6 we also plot the broad line FWHM with stellar mass and compare our results with recent similar observations of broad Hα in $z = 1$–2 galaxies and AGNs from Newman et al. (2012a) and Genzel et al. (2014) along with those from Martin et al. 2014. This shows how the Hα FWHM increases with stellar mass (and star formation rate). (see also Förster Schreiber et al. 2018; Freeman et al. 2017). As well as the broad Hα line width, in Fig. 6 we also show the broad / narrow Hα flux ratio ($f_{\mathrm{broad}}\,/\,f_{\mathrm{narrow}}$) as a function of star-formation rate, star formation surface density and stellar mass. We will combine the broad Hα luminosities and line-widths in the next section to determine what the trends of increasing FWHM with stellar mass and star formation rate seen in Fig. 6 imply for the outflow energetics.

3.2 Outflow Properties: estimates of mass, energy and momentum

The ionised gas mass (i.e. the gas that is emitting the Hα) can be estimated assuming an electron temperature

$T = 10^4$ K following Osterbrock & Ferland 2006 using the relation

$$\frac{M_{\mathrm{gas}}}{2.38 \times 10^8\,\mathrm{M_\odot}} = \left(\frac{L_{H\alpha}}{10^{43}\,\mathrm{erg\,s^{-1}}}\right)\left(\frac{n_e}{100\,\mathrm{cm^{-3}}}\right)^{-1} \quad (1)$$

This relation has been used in a number of studies of galaxies involving Hα (or Hβ) emission, although the normalisation of the co-efficient varies depending on the choice of assumptions (Holt et al. 2006; Genzel et al. 2011; Liu et al. 2013; Rodríguez Zaurín et al. 2013; Harrison et al. 2014). Since we do not have Hβ measurements for this sample (to correct for the dust extinction in the emission lines), we adopt a simple approach to correct the observed broad Hα luminosity to total Hα luminosity. For simplicity, we adopt the median reddening for the KROSS sample (derived from the best-fit SED to the broad-band photometry; A$_\mathrm{v} = 1.10 \pm 0.07$; Harrison et al. 2017), and use the relation between stellar and gas-phase reddening from Wuyts et al. (2013); $A_\mathrm{gas} = A_\mathrm{v} \times (1.9 - 0.15\,A_\mathrm{v})$. This calibration suggest an average gas-phase extinction at Hα of $A_{H\alpha} = 2.0 \pm 0.1$ which is also consistent with the estimates from the far-infrared (e.g. Thomson et al. 2017). For the

stack of all galaxies in our sample, we estimate an average ionised gas mass in the outflow of $M_{gas} = 1–6 \times 10^8\,M_\odot$ assuming $n_e = 75\,cm^{-3}$ (as derived from the [S$\scriptstyle II$] doublet emission line ratio in § 2.4). We note that this mass should be considered a lower limit since the ionised gas will only make up a fraction of the *total* out-flowing gas content.

After estimating the mass in the outflow, we estimate the kinetic energy in the outflow as $E_{kin} = 0.5\,M_{gas}\,v_{gas}^2$. Following Harrison et al. (2014) and Liu et al. (2013) we assume that all of the ionised gas in the broad component is involved in the outflow, with a bulk flow velocity of $v_{gas} = FWHM_{H\alpha}\,/\,2$ (suitable for a wide-angle bi-cone outflow or spherically symmetric model). For the composite stack in Fig. 2, this leads to a kinetic energy of (1–8) $\times 10^{56}$ erg. Assuming a maximum spatial extent of 10 kpc (Fig. 3) and a continuous outflow, the outflow time is $t_{wind} \sim 40\,Myr$ and consequently the outflow kinetic energy rate is $\dot{E}_{kin} = (0.8–6) \times 10^{41}\,erg\,s^{-1}$.

The inferred mass outflow rate can be expressed in terms of the broad Hα luminosity and line width, electron density and spatial extent as

$$\frac{dM}{dt}\left(\frac{M_\odot}{yr^{-1}}\right) = 0.024 \left(\frac{L_{H\alpha}}{10^{43}\,erg\,s^{-1}}\right)\left(\frac{n_e}{100\,cm^{-3}}\right)^{-1} \times$$
$$\left(\frac{FWHM_{H\alpha}}{km\,s^{-1}}\right)\left(\frac{10\,kpc}{r}\right) \quad (2)$$

For our sample, this suggests a mass outflow rate, $dM_{wind}\,/\,dt = 3–18\,M_\odot\,yr^{-1}$ (and so a mass outflow rate per unit star formation rate of $dM_{wind}\,/\,dt\,/SFR$ less than unity). An alternative approach is to assume a spherical volume of out-flowing ionised gas which gives a mass outflow rate of $\dot{M}_{wind} = 3\,M_{gas}\,v_{wind}\,/\,r$ and $\dot{E}_{kin} = 0.5\,\dot{M}\,(v_{wind}^2 + \sigma^2)$ where σ is the velocity dispersion and v_{wind} is the outflow velocity. To match local samples as closely as possible (e.g. Rodríguez Zaurín et al. 2013), we adopt $v_{wind} = FWHM\,/\,2$, the velocity dispersion to be $\sigma = FWHM\,/\,2.355$, the maximum extent of the outflow to be a radius $< 10\,kpc$ and again use $n_e = 75\,cm^{-3}$. Using this approach, we obtain a mass outflow rate of $\dot{M}_{wind} = 1–8\,M_\odot\,yr^{-1}$ and $\dot{E}_{kin} = (3–8) \times 10^{40}\,erg\,s^{-1}$. This range in outflow kinetic energy rate is in agreement with the range of values using the first method. Although we caution that there are potentially significant systematic uncertainties in our estimates (e.g. see also Harrison et al. 2018), these mass outflow rates and kinetic energy estimates are similar to those derived for local starbursts using absorption line studies for galaxies with comparable far-infrared luminosities to those studied here (Heckman et al. 2000). However, we re-iterate that both methods we employ are likely to provide lower limits on the total mass of the outflow as we are only observing the line-emitting (ionised) gas. Most of the outflow is likely to be in the atomic or molecular phases that are cooler than the ionised material (Rupke et al. 2005; Rupke & Veilleux 2013; Walter et al. 2002). Hence the total mass involved in the outflow could be much higher (see also e.g. Greene et al. 2011).

We examine how the radiation pressure and supernovae energy compare to the energy in the outflows. First, we assume that the energy from supernovae per solar mass of stars formed per year is $1 \times 10^{49}\,erg\,yr^{-1}$ (applicable for stellar ages $\gtrsim 40\,Myr$ and following Leitherer et al. 1999; Veilleux

et al. 2005)[1]. Thus, for our composite sample with a median star-formation rate of $SFR = 7 \pm 1\,M_\odot\,yr^{-1}$, the total energy available from SNe is $\sim 7 \times 10^{49}$ erg, and the coupling efficiency of the SNe to the wind is $\epsilon_{SNe} = 0.7–3\%$. We also compare the momentum rate in the outflow ($\dot{P}$) to the radiation momentum rate ($L\,/\,c$). The average infrared luminosity for the full sample (measured from the stacked *Herschel*\,/\,PACS+SPIRE photometry; e.g. Stott et al. 2016) is $L_{IR} \sim 1 \times 10^{11}\,L_\odot$, which suggests a radiative momentum flux rate of $L_{IR}\,/\,c = (6 \pm 2) \times 10^{35}\,erg\,m^{-1}$. In comparison to the momentum rate of the outlow (with $\dot{P} = \dot{M}_{wind}$), the momentum ratio is in the range $\dot{P}\,/\,L_{IR} = 7–600$ (with a median of $\dot{P}\,/\,L_{IR} = 27$), and thus not indicative of momentum driven outflows (Dekel & Krumholz 2013).

3.3 Outflow Properties: dependence on mass and star formation rate

Whilst it is useful to estimate the energetics of the outflows in the full sample of 529 galaxies, there are significant systematic uncertainties in the absolute values derived. However, numerical models suggest that the outflow energetics scale (non linearly) with circular velocity, star formation and gas density (e.g. Hopkins et al. 2012; Barai et al. 2015), and so a useful test can be performed by comparing these quantities between sub-samples as a function of stellar mass and star-formation rate. An in §2, we therefore sub-divide the stacks in to smaller subsamples to investigate how the energetics of the wind (kinetic energy, mass loading) depend on galaxy properties to test the predictions of the superwind theory – that the energetics of the wind should correlate with the star-formation rate of the galaxy.

In Fig. 7 we show how the physical properties of the outflows correlate as a function of galaxy properties derived using the line widths and luminosities from Fig. 6 (see also Table 2). First we derive the mass outflow rate as a function of star-formation rate and overlay those calculated for high-redshift star-forming galaxies by Genzel et al. (2014) (which are also derived using the broad lines from composite spectra around the redshifted Hα) and those for DEEP 2 galaxies from Martin et al. (2012). To be consistent with our sample, from the SINS+KMOS^{3D} comparison sample from Genzel et al. we exclude (candidate) AGNs and/or galaxies with [N$\scriptstyle II$]\,/\,H$\alpha > 0.7$ and adopt a maximum spatial extent for the outflow of $2 \times HWHM$. Fig. 7 shows an increasing trend of mass outflow rate, $dM\,/\,dt$ with star-formation rate. The scaling between star-formation rate and mass outflow rate suggested by the data, $dM\,/\,dt \propto SFR^{0.86\pm0.15}$ is consistent with predictions from hydrodynamical models, which predict a sub-linear power-law relation ($\dot{M}_{wind} \propto \dot{M}_\star^{0.7}$) that implies a lower efficiency at higher star-formation rates (Hopkins et al. 2012). We also plot the relation between mass outflow rate and stellar mass in Fig. 7 which also shows a sub-linear trend increasing with increasing mass. The scaling between stellar mass and mass outflow rate is $dM\,/\,dt \propto SFR^{0.34\pm0.14}$, which is also similar to the predictions from Hopkins et al. (2012), $\dot{M}_{wind} \propto \dot{M}_\star^{0.49}$.

The dependence of the mass loading ($dM\,/\,dt\,/\,SFR$)

---

[1] If we instead used the supernovae energy from Dalla Vecchia & Schaye (2008), these values would be a factor $\sim 2\times$ lower.
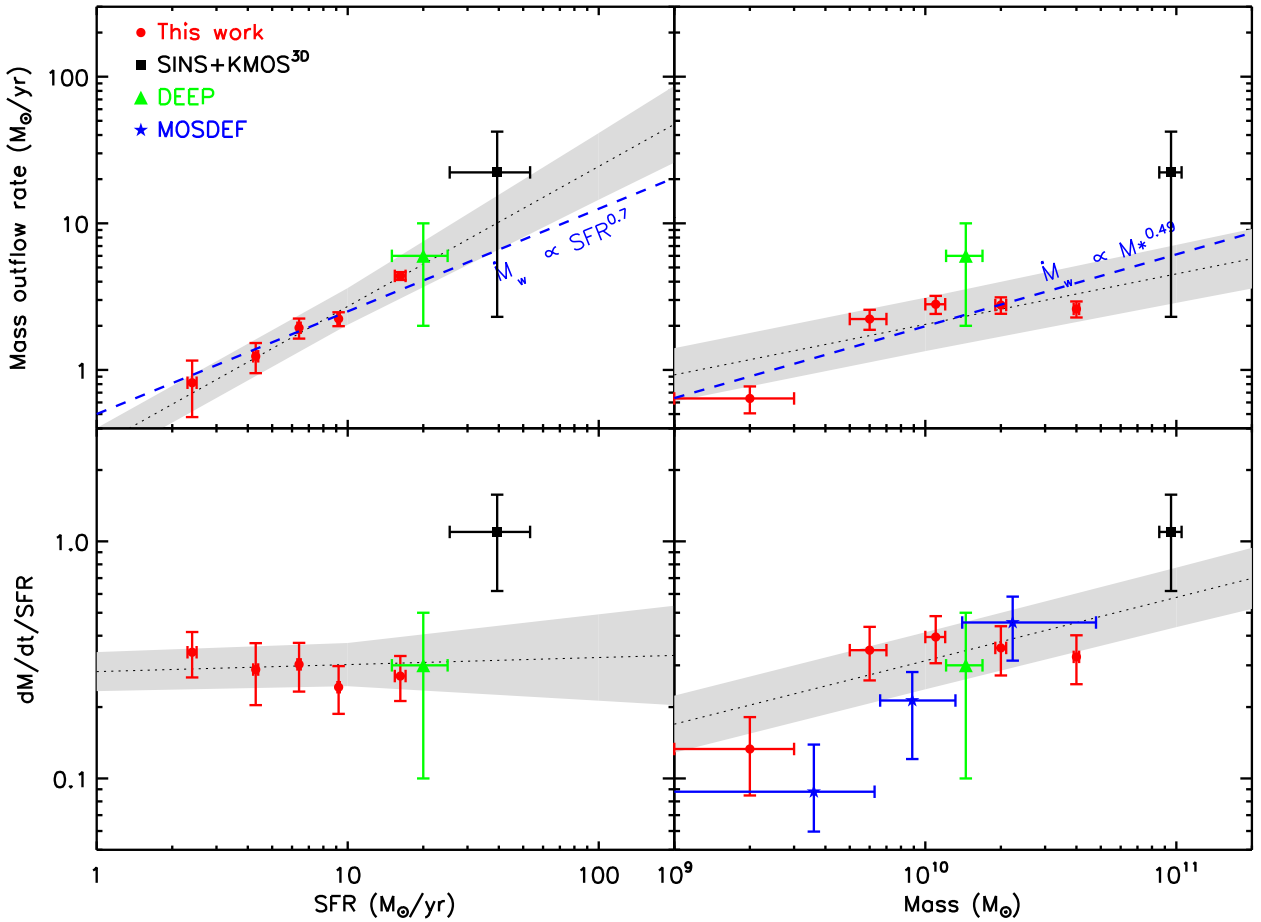
Figure 7. Inferred physical properties of the outflow as a function of galaxy properties. *Top Left:* Mass outflow rate as a function of star formation rate for the galaxies in our sample. The bins of star-formation rate are defined by equal numbers of galaxies per bin (see Table 1). We also overlay the estimates of the mass outflow rates for high-redshift star-forming galaxies from Genzel et al. (2014) and Freeman et al. (2017) (both of which are also derived using the broad lines from composite spectra around the redshifted Hα). For consistency with our data, we have scaled the mass outflow rates from Freeman et al. (2017) to the same spatial extent as those assumed in our observations. We also include the measurements from Martin et al. (2012) for high-redshift star-forming galaxies from the DEEP2 survey. The data appear to show a trend of increasing mass outflow rate with star-formation rate with the form $dM/dt \propto \mathrm{SFR}^{0.86 \pm 0.15}$ (dotted-line plus grey region), which is consistent with model predictions from Hopkins et al. (2012) which has the form $\dot{M}_{\mathrm{wind}} \propto \mathrm{SFR}^{0.7}$. *Top Right:* Mass outflow rate as a function of stellar mass (with each stellar mass bin containing equal numbers of galaxies). The trend of increasing mass outflow rate with stellar mass following $\dot{M}_{\mathrm{wind}} \propto M_{\star}^{0.49}$ from Hopkins et al. (2012) is in reasonable agreement with the data, which suggest $dM/dt \propto \mathrm{SFR}^{0.34 \pm 0.14}$ (dotted line). *Bottom Left:* Mass loading ($\dot{M}_{\mathrm{wind}}/\mathrm{SFR}$) as a function of star formation rate. The average mass loading is approximately constant over the star-formation rate range of our data, with $dM/dt/\mathrm{SFR} = 0.3 \pm 0.1$ and $dM/dt/\mathrm{SFR} \propto \mathrm{SFR}^{-0.07 \pm 0.14}$. *Bottom Right:* The mass loading as a function of stellar mass. In the fit, we include all of our data-points as well as the comparison samples in the fit, and identify a (weak) trend of increasing mass outflow rate with stellar mass. The mass loading has a scaling with $dM/dt/\mathrm{SFR} \propto M_{\star}^{0.26 \pm 0.07}$.

on stellar mass or star formation is less significant. Fig. 7 shows that the mass loading is approximately constant over star-formation rate range of our data, with $dM/dt/\mathrm{SFR} = 0.3 \pm 0.1$, although there appears to be a weak dependence on stellar mass, with $dM/dt/\mathrm{SFR} \propto M_{\star}^{0.26 \pm 0.07}$. In the latter fit, we also include similar constraints for $z \sim 1$ star forming galaxies from the recent MOSDEF survey from Freeman et al. (2017) (who also measure the underlying Hα broad emission line properties). We note however that for consistency, we have scaled their derived mass outflow rates to assume the same spatial extent as our data.

Finally, we attempt to infer the fate of the outflow-

ing gas by investigating whether the outflows have sufficient speed to escape the gravitational potential of the galaxies, or whether the gas is likely to return to the galactic disk as a "fountain" flow. For an isothermal gravitational potential that extends to a maximum radius r_{max} and has a circular velocity v_{c}, the escape velocity at a radius r is given by:

$$v_{\mathrm{esc}} = (2\,v_{\mathrm{c}}^2\,[1 + \ln(r_{\mathrm{max}}/r)])^{0.5} \qquad (3)$$

Thus, $v_{\mathrm{esc}} = 2.5\,v_{\mathrm{c}}$ for $r_{\mathrm{max}}/r \sim 9$ (i.e. $r_{\mathrm{max}} = 100\,\mathrm{kpc}$ and $r = 10\,\mathrm{kpc}$). In Fig. 8 we show the broad (and narrow) line Hα FWHM as a function of (inclination corrected) circular velocity for the galaxies in our sample. This figure shows
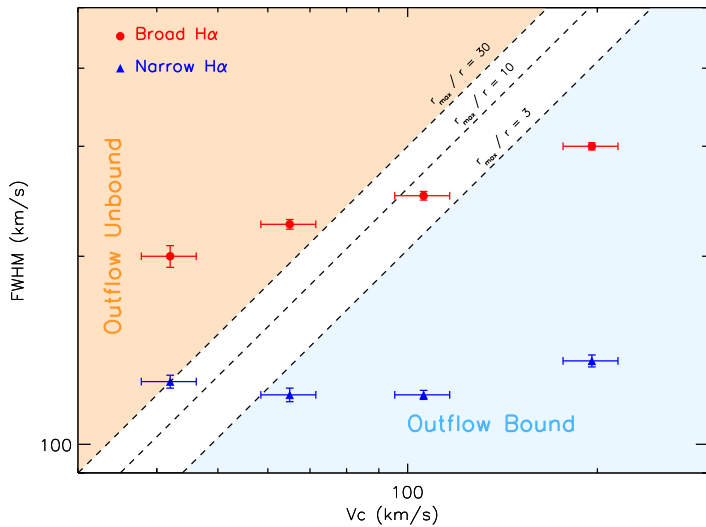
Figure 8. FWHM of the broad- and narrow- line Hα as a function of (inclination corrected) circular velocity. The dashed lines denote the gas velocity required to escape the gravitational potential assuming an isothermal gravitation potential that extends to a maximum radius of r_{max} and has a virial velocity v_c at radius r. The escape velocity is given by $v_{esc} = (2\,v_c^2(1 + ln(r_{max}/r)))^{0.5}$ and in the plot we show three values of $r_{max}\,/\,r = 3$, 10 and 30. Above $r_{max}\,/\,r = 30$, the outflowing gas is likely to escape the gravitational potential of the galaxy, and the lowest mass galaxies in our sample (identified by the lowest circular velocity, V_c) meet this criteria. In contrast, in the highest mass (highest V_c) galaxies, the outflow does not appear to have sufficient velocity to escape the potential and will be retained.

the FWHM of the broad Hα increases with circular velocity, and we derive a scaling FWHM $\propto v_c^{0.21\,\pm\,0.05}$. This scaling is significantly sub-linear and, as Fig. 8 shows, the galaxies with lowest v_c (shallower potentials) have gas with FWHM greater than our estimates of the velocity required to escape the galaxy. Conversely those at higher v_c (and hence higher mass and deeper potentials) have gas with FWHM that is below that required to escape the galaxy. Of course, here we are comparing the FWHM of the broad line with the escape velocity required for a single cloud of gas, and therefore some care must be taken when comparing these quantities outright. Nevertheless, a significant fraction of the gas in the lowest mass galaxies should have sufficient velocity to escape the gravitational potential, whilst in the highest mass galaxies, most of the gas will be retained, most likely flowing back on to the galaxy disk (as also can also be seen in Fig. 6).

4 CONCLUSIONS

By exploiting KMOS observations of 529 star-forming galaxies at $z \sim 1$, we have investigated the average properties of starburst driven, galaxy-scale outflows. Our sample spans a range of mass and star-formation rate, from $M_\star = 0.5$–$5 \times 10^{10}\,M_\odot$ and SFR = 1.5–28 $M_\odot\,yr^{-1}$. We measure the two dimensional velocity field for each galaxy, model and subtract the galaxy dynamics, and then stack the rest-frame optical spectra to search for and measure the properties of the underlying, broad Hα emission. We identify broad Hα

emission along with forbidden lines of [NII] and [SII]. The presence of broad forbidden lines suggests that the outflows are not confined to a broad line region around an AGN (and indeed, we remove galaxies in our sample that display AGN characteristics in their optical spectra, mid-infrared colours or X-ray emission). We show that the broad emission is spatially extended across at least 10 kpc in projection.

The composite spectra has a reddening corrected star-formation rate SFR = 7 $M_\odot\,yr^{-1}$ and $M_\star = (0.9 \pm 0.1) \times 10^{10}\,M_\odot$, and from the broad Hα we derive mass outflow rates of 2–10 $M_\odot\,yr^{-1}$. By comparing the kinetic energy in the wind with the energy released by supernovae, we estimate a coupling efficiency of $\lesssim 3\%$. This coupling efficiency is also comparable to that between the radiation pressure from star formation, suggesting that both the radiation pressure and SNe have sufficient energy or momentum to drive the outflow (if they are able to couple $\sim 3\%$ of their energy to the gas). Although there are systematic uncertainties in these mass outflow rates depending on the assumptions made, these coupling efficiencies are much less than unity and suggest that either the supernovae or radiation pressure should be able to drive the outflow.

We also investigate the dependence of wind energetics with global galaxy properties (mass and star formation). Although the data are limited by the sample size per bin (and systematics in deriving physical parameters), we show that the mass outflow rates increases with star-formation rate and mass with $dM\,/\,dt \propto SFR^{0.86\pm0.15}$ and $dM\,/\,dt \propto SFR^{0.34\pm0.14}$. Both of these scalings are consistent with predictions from hydrodynamical models which predict sub-linear power-law relations of $dM\,/\,dt \propto \dot{M}_\star^{0.49}$ (Hopkins et al. 2012). However, the mass loading of the winds ($\dot{M}_{wind}\,/\,SFR$) shows little dependence on star formation rate (over the range covered by our data), although we identify a weak trend with stellar mass such that $dM\,/\,dt\,/\,SFR \propto M_\star^{0.26\pm0.07}$.

We investigate whether the outflows have sufficient speed to escape the gravitational potential of the galaxies, or whether the gas is more likely return to the galactic disk as a fountain flow. The line width of the broad Hα increases with disk circular velocity with a sub-linear scaling relation FWHM $\propto v_c^{0.21\,\pm\,0.05}$. In the lowest mass galaxies, $M \lesssim 10^{10}\,M_\odot$ a significant fraction of the gas should have sufficient velocity to escape the gravitational potential, whilst in the highest mass galaxies, most of the gas will be retained, most likely flowing back on to the galaxy disk at later times.

These results are based on average values for (sub)-populations binned by mass, star-formation rate, or circular velocity. Of course, there are likely to be variations in individual objects in terms of (e.g.) sizes, mass, star formation rate or electron densities (e.g. Rose et al. 2018). To make the same measurements in individual galaxies will require extremely deep exposures ($\gtrsim 100$ hr) per galaxy, which the next generation of (upcoming) KMOS surveys should provide.

REFERENCES

Alexander, D. M., Swinbank, A. M., Smail, I., McDermid, R., & Nesvadba, N. P. H. 2010, MNRAS, 402, 2211

Barai, P., Monaco, P., Murante, G., Ragagnin, A., & Viel, M. 2015, MNRAS, 447, 266

Benson, A. J., Bower, R. G., Frenk, C. S., Lacey, C. G., Baugh, C. M., & Cole, S. 2003, ApJ, 599, 38

Bordoloi, R., Lilly, S. J., Knobel, C., Bolzonella, M., Kampczyk, P., Carollo, C. M., Iovino, A., & Zucca, E. et al. 2011, ApJ, 743, 10

Bower, R. G., Benson, A. J., & Crain, R. A. 2012, MNRAS, 422, 2816

Bruzual, G. & Charlot, S. 2003, MNRAS, 344, 1000

Chabrier, G. 2003, PASP, 115, 763

Chen, Y.-M., Tremonti, C. A., Heckman, T. M., Kauffmann, G., Weiner, B. J., Brinchmann, J., & Wang, J. 2010, AJ, 140, 445

Cole, S., Lacey, C. G., Baugh, C. M., & Frenk, C. S. 2000, MNRAS, 319, 168

Creasey, P., Theuns, T., & Bower, R. G. 2013, MNRAS, 429, 1922

Dahlem, M., Petr, M. G., Lehnert, M. D., Heckman, T. M., & Ehle, M. 1997, A&A, 320, 731

Dalla Vecchia, C. & Schaye, J. 2008, MNRAS, 387, 1431

Dekel, A. & Krumholz, M. R. 2013, MNRAS, 432, 455

Donley, J. L., Koekemoer, A. M., Brusa, M., Capak, P., Cardamone, C. N., Civano, F., Ilbert, O., Impey, C. D., Kartaltepe, J. S., Miyaji, T., Salvato, M., Sanders, D. B., Trump, J. R., & Zamorani, G. 2012, ApJ, 748, 142

Erb, D. K., Steidel, C. C., Shapley, A. E., Pettini, M., Reddy, N. A., & Adelberger, K. L. 2006, ApJ, 647, 128

Förster Schreiber, N. M., Übler, H., Davies, R. L., Genzel, R., Wisnioski, E., Belli, S., Shimizu, T., & Lutz, D. et al. 2018, ArXiv:1807.04738

Freeman, W. R., Siana, B., Kriek, M., Shapley, A. E., Reddy, N., Coil, A. L., Mobasher, B., & Muratov, A. L. et al. 2017, ArXiv:1710.03230

Genzel, R., Förster Schreiber, N. M., Rosario, D., Lang, P., Lutz, D., Wisnioski, E., Wuyts, E., & Wuyts, S. et al. 2014, ApJ, 796, 7

Genzel, R., Newman, S., Jones, T., Förster Schreiber, N. M., Shapiro, K., Genel, S., Lilly, S. J., & Renzini, A. et al. 2011, ApJ, 733, 101

Greene, J. E., Zakamska, N. L., Ho, L. C., & Barth, A. J. 2011, ApJ, 732, 9

Harrison, C. M., Alexander, D. M., Mullaney, J. R., Stott, J. P., Swinbank, A. M., Arumugam, V., Bauer, F. E., Bower, R. G., Bunker, A. J., & Sharples, R. M. 2016, MNRAS, 456, 1195

Harrison, C. M., Alexander, D. M., Mullaney, J. R., & Swinbank, A. M. 2014, MNRAS, 441, 3306

Harrison, C. M., Costa, T., Tadhunter, C. N., Flütsch, A., Kakkad, D., Perna, M., & Vietri, G. 2018, Nature Astronomy, 2, 198

Harrison, C. M., Johnson, H. L., Swinbank, A. M., Stott, J. P., Bower, R. G., Smail, I., Tiley, A. L., & Bunker, A. J. et al. 2017, MNRAS, 467, 1965

Heckman, T. M., Armus, L., & Miley, G. K. 1990, ApJS, 74, 833

Heckman, T. M., Lehnert, M. D., Strickland, D. K., & Armus, L. 2000, ApJS, 129, 493

Holt, J., Tadhunter, C. N., & Morganti, R. 2006, Astronomische Nachrichten, 327, 147

Hopkins, P. F., Quataert, E., & Murray, N. 2012, MNRAS, 421, 3522

Johnson, H. L., Harrison, C. M., Swinbank, A. M., Tiley, A. L., Stott, J. P., Bower, R. G., Smail, I., & Bunker, A. J. et al. 2018, MNRAS, 474, 5076

Kereš, D., Katz, N., Davé, R., Fardal, M., & Weinberg, D. H. 2009, MNRAS, 396, 2332

Kewley, L. J., Groves, B., Kauffmann, G., & Heckman, T. 2006, MNRAS, 372, 961

Krumholz, M. R. & Thompson, T. A. 2013, MNRAS, 434, 2329

Lehnert, M. D. & Heckman, T. M. 1996, ApJ, 462, 651

Lehnert, M. D., Le Tiran, L., Nesvadba, N. P. H., van Driel, W., Boulanger, F., & Di Matteo, P. 2013, A&A, 555, A72

Leitherer, C., Schaerer, D., Goldader, J. D., Delgado, R. M. G., Robert, C., Kune, D. F., de Mello, D. F., Devost, D., & Heckman, T. M. 1999, ApJS, 123, 3

Liu, G., Zakamska, N. L., Greene, J. E., Nesvadba, N. P. H., & Liu, X. 2013, MNRAS, 436, 2576

Luo, B., Bauer, F. E., Brandt, W. N., Alexander, D. M., Lehmer, B. D., Schneider, D. P., Brusa, M., & Comastri et al., A. 2008, ApJS, 179, 19

Martin, C. L. 2005, ApJ, 621, 227

Martin, C. L., Shapley, A. E., Coil, A. L., Kornei, K. A., Bundy, K., Weiner, B. J., Noeske, K. G., & Schiminovich, D. 2012, ApJ, 760, 127

Martin, D. C., Chang, D., Matuszewski, M., Morrissey, P., Rahman, S., Moore, A., Steidel, C. C., & Matsuda, Y. 2014, ApJ, 786, 107

McCray, R. & Kafatos, M. 1987, ApJ, 317, 190

Meyer, D. M. & York, D. G. 1987, ApJL, 315, L5

Murray, N., Quataert, E., & Thompson, T. A. 2005, ApJ, 618, 569

—. 2010, ApJ, 709, 191

Newman, S. F., Genzel, R., Förster-Schreiber, N. M., Shapiro Griffin, K., Mancini, C., Lilly, S. J., Renzini, A., & Bouché, N. et al. 2012a, ApJ, 761, 43

Newman, S. F., Shapiro Griffin, K., Genzel, R., Davies, R., Förster-Schreiber, N. M., Tacconi, L. J., Kurk, J., & Wuyts, S. et al. 2012b, ApJ, 752, 111

Osterbrock, D. E. 1989, Astrophysics of gaseous nebulae and active galactic nuclei

Osterbrock, D. E. & Ferland, G. J. 2006, Astrophysics of gaseous nebulae and active galactic nuclei

Osterbrock, D. E. & Shuder, J. M. 1982, ApJS, 49, 149

Pettini, M., Rix, S. A., Steidel, C. C., Adelberger, K. L., Hunt, M. P., & Shapley, A. E. 2002, ApJ, 569, 742

Queyrel, J., Contini, T., Kissler-Patig, M., Epinat, B., Am-

ram, P., Garilli, B., Le Fèvre, O., Moultaka, J., Paioro, L., Tasca, L., Tresse, L., Vergani, D., López-Sanjuan, C., & Perez-Montero, E. 2012, A&A, 539, A93

Rodríguez Zaurín, J., Tadhunter, C. N., Rose, M., & Holt, J. 2013, MNRAS, 432, 138

Rose, M., Tadhunter, C., Ramos Almeida, C., Rodríguez Zaurín, J., Santoro, F., & Spence, R. 2018, MNRAS, 474, 128

Rupke, D. S., Veilleux, S., & Sanders, D. B. 2002, ApJ, 570, 588

—. 2005, ApJS, 160, 115

Rupke, D. S. N. & Veilleux, S. 2013, ApJL, 775, L15

Saintonge, A., Kauffmann, G., Kramer, C., Tacconi, L. J., Buchbender, C., Catinella, B., Fabello, S., & Graciá-Carpio, J. et al. 2011, MNRAS, 415, 32

Simcoe, R. A., Sargent, W. L. W., & Rauch, M. 2004, ApJ, 606, 92

Somerville, R. S. & Primack, J. R. 1999, MNRAS, 310, 1087

Spergel, D. N., Bean, R., Doré, O., Nolta, M. R., Bennett, C. L., Dunkley, J., Hinshaw, G., & Jarosik, N. et al. 2007, ApJS, 170, 377

Springel, V. & Hernquist, L. 2003, MNRAS, 339, 312

Steidel, C. C., Erb, D. K., Shapley, A. E., Pettini, M., Reddy, N., Bogosavljević, M., Rudie, G. C., & Rakic, O. 2010, ApJ, 717, 289

Stern, D., Eisenhardt, P., Gorjian, V., Kochanek, C. S., Caldwell, N., Eisenstein, D., Brodwin, M., Brown, M. J. I., Cool, R., Dey, A., Green, P., Jannuzi, B. T., Murray, S. S., Pahre, M. A., & Willner, S. P. 2005, ApJ, 631, 163

Stott, J. P., Sobral, D., Swinbank, A. M., Smail, I., Bower, R., Best, P. N., Sharples, R. M., Geach, J. E., & Matthee, J. 2014, MNRAS, 443, 2695

Stott, J. P., Swinbank, A. M., Johnson, H. L., Tiley, A., Magdis, G., Bower, R., Bunker, A. J., & Harrison, C. M. et al. 2016, MNRAS, 457, 1888

Thomson, A. P., Simpson, J. M., Smail, I., Swinbank, A. M., Best, P. N., Sobral, D., Geach, J. E., Ibar, E., & Johnson, H. L. 2017, ApJ, 838, 119

Turner, O. J., Cirasuolo, M., Harrison, C. M., McLure, R. J., Dunlop, J. S., Swinbank, A. M., Johnson, H. L., Sobral, D., Matthee, J., & Sharples, R. M. 2017, MNRAS, 471, 1280

Veilleux, S., Cecil, G., & Bland-Hawthorn, J. 2005, ARAA, 43, 769

Walter, F., Weiss, A., & Scoville, N. 2002, ApJL, 580, L21

Westmoquette, M. S., Clements, D. L., Bendo, G. J., & Khan, S. A. 2012, MNRAS, 424, 416

White, S. D. M. & Frenk, C. S. 1991, ApJ, 379, 52

Wisnioski, E., Förster Schreiber, N. M., Wuyts, S., Wuyts, E., Bandara, K., Wilman, D., Genzel, R., & Bender, R. e. a. 2015, ApJ, 799, 209

Wuyts, S., Förster Schreiber, N. M., Nelson, E. J., van Dokkum, P. G., Brammer, G., Chang, Y.-Y., Faber, S. M., & Ferguson, H. C. et al. 2013, ApJ, 779, 135

Yuan, T.-T., Kewley, L. J., Swinbank, A. M., Richard, J., & Livermore, R. C. 2011, ApJL, 732, L14

APPENDIX A: MASS OUTFLOW RATES AS A FUNCTION OF MASS AND STAR FORMATION RATE

Table A1 provides our estimates of the mass outflow rates and their energetics as a function of stellar mass and star formation rate. These are calculated using the extinction corrected, broad line Hα luminosity and FWHM as discuss in section 3.2.

Table A1. Derived Properties of the Outflows as a function of star formation rate and stellar mass

Stack	M_{wind} $(10^8\,\mathrm{M_\odot})$	$\mathrm{d}M_{\mathrm{wind}}\,/\,\mathrm{d}t$ $(\mathrm{M_\odot}\,\mathrm{yr}^{-1})$	$\mathrm{d}M_{\mathrm{wind}}\,/\,\mathrm{d}t\,/\,\mathrm{SFR}$	$E_{\mathrm{k,wind}}$ $(10^{54}\,\mathrm{erg})$	$E(\mathrm{SNe})\,/\,E_{\mathrm{k,wind}}$ (%)	$(L\,/\,c)\,/\,\dot{P}$ (%)
All	0.89 ± 0.06	2.53 ± 0.54	0.38 ± 0.08	70 ± 2	2.9 ± 0.6	0.4 ± 0.1
SFR-1	0.44 ± 0.03	0.82 ± 0.17	0.34 ± 0.07	15 ± 1	1.1 ± 0.2	0.6 ± 0.1
SFR-2	0.60 ± 0.13	1.24 ± 0.36	0.29 ± 0.08	25 ± 1	1.2 ± 0.3	0.7 ± 0.2
SFR-3	0.83 ± 0.10	1.94 ± 0.45	0.30 ± 0.07	44 ± 2	1.6 ± 0.4	0.5 ± 0.1
SFR-4	0.89 ± 0.10	2.23 ± 0.51	0.24 ± 0.06	54 ± 2	1.5 ± 0.4	0.6 ± 0.1
SFR-5	1.55 ± 0.10	4.38 ± 0.92	0.27 ± 0.06	120 ± 15	2.1 ± 0.5	0.5 ± 0.1
Mass-1	0.35 ± 0.10	0.64 ± 0.22	0.13 ± 0.05	11 ± 1	0.4 ± 0.2	1.6 ± 0.6
Mass-2	1.11 ± 0.16	2.22 ± 0.55	0.35 ± 0.09	43 ± 1	1.4 ± 0.3	0.6 ± 0.1
Mass-3	1.30 ± 0.03	2.80 ± 0.57	0.39 ± 0.09	59 ± 2	1.8 ± 0.4	0.5 ± 0.1
Mass-4	0.98 ± 0.06	2.77 ± 0.58	0.36 ± 0.08	76 ± 3	2.7 ± 0.6	0.4 ± 0.1
Mass-5	0.79 ± 0.06	2.61 ± 0.56	0.33 ± 0.08	83 ± 3	3.4 ± 0.8	0.5 ± 0.1

Notes: Error-bars reflect uncertainties on the line fits.